Research Article | DOI:10.5281/zenodo.12540643
www.jnanosam.com

NANOSAM
Journal of NanoScience in Advanced Materials

Structural, Magnetic, Electrical and Dielectric Characterizations of $Co_{0.5}Ni_{0.5}FeCuO_4$ Ferrite

Ahlem Cherif [1#], Nadia Zaidi[1] and Hayet Saghrouni[2]

The $Co_{0.5}Ni_{0.5}FeCuO_4$ compound was elaborated using sol-gel reaction route. X-ray diffraction patterns indicated that the sample crystallize in the cubic spinel structure (Fd-3m space group). Magnetic measurements revealed that the prepared sample showed a paramagnetic-ferromagnetic transition at T_C= 785 K. Then, dielectric data has been carried out by means of impedance spectroscopy in a wide frequency and temperature ranges. For the sample, the activation energy E_a estimated from the slope of the linear fit plot is equal to 0.42 eV at temperature range 200-420 K. The electrical modulus and impedance studies reveal the presence of a relaxation phenomenon with non-Debye type in the prepared sample. Nyquist representation (Z″ vs. Z') was plotted and their characteristic behavior was analyzed in terms of electrical equivalent circuit.

1. Introduction

The spinel ferrites are important magnetic oxide materials found in technological and industrial applications with various advantages in terms of electrical and magnetic properties. The excellent properties of these materials, such as their high electrical resistivity, high saturation magnetization, high permeability, low eddy current, dielectric loss, etc. make them suitable for various applications. They are widely used in microwave devices, drug delivery applications, electrical generators, magnetic diagnosis, spintronics etc. Spinel ferrites also used as catalyst in numerous chemical reactions such as alkylation [1]. The magnetic and electrical behavior of these oxides depends upon nature of substituted element, size of the particle and ionic radii of substituent [2]. In the crystal geometry of these materials, two kinds of interstitial spaces occur, named by tetrahedral (A) and octahedral (B) sites which are surrounded by 4 and 6 oxygen ions respectively. The properties of ferrite mainly depend upon the cations distributions over these available sites [3-4]. The magnetic behavior of ferrites is based on the three types of super-exchange interactions A-B, A-A and B-B mediated by the intermediate O^{2-} ions. Much research has been done on metal ions substituted spinel ferrites [5]. The well-known category of spinel ferrites, $CoFe_2O_4$ has attracted the interest of researchers due to its many valuable properties such as high chemical stability, remarkable mechanical hardness, moderate saturation magnetization and high coercivity. The properties of $CoFe_2O_4$ can be modified by addition of various divalent and trivalent metal ions as required [6-9]. Low electrical conductivity and low dielectric losses are desirable for ferrites operating at high frequency leading to their frequent use in the manufacture of microwave devices. Currently, controlling the electrical conductivity of ferrites is a challenging issue. Therefore, for a particular application and controlled electrical conductivities the preferred structural and magnetic properties of the spinel ferrites may be tailored by synthesis conditions and sum of substituent into the spinel lattice. For each synthesis method, the structure and properties of the obtained device were controlled by the annealed temperature. So the magnetic and electrical properties of these ferrites type could be strongly influenced by fabrication methods steps, annealing temperature and structural properties such as grain size, porosity and crystallite size.

In the scope of this work the sol-gel method was carried out to prepare $Co_{0.5}Ni_{0.5}FeCuO_4$ ferrite system. Structural, electrical, dielectric and magnetic properties of this sample were successively investigated. Therefore, in this paper,

[1]*Department of Physics, College of Sciences, Jouf University, Aljouf, Saudi Arabia.*[2]*Physics Department, Faculty of Science and Art in Baljurashi , AL-Baha University, Al Bahah, Saudi Arabia.*
#Corresponding author: amnajima@ju.edu.sa

Keywords: Spinel ferrite; Activation energy; Modulus; Nyquist representation; relaxation phenomenon.

Received: 05 February 2024 | Accepted: 01 June 2024 | Published online: 30 June 2024

NANOSAM
Journal of NanoScience in Advanced Materials

we focus on the effect of grain and grain boundary on the electrical and dielectric proprieties of $Co_{0.5}Ni_{0.5}FeCuO_4$ which is synthesized by sol–gel combustion process.

2. Results and Discussion

2.1. Structural Properties

The powder X-ray diffraction pattern of the $Co_{0.5}Ni_{0.5}FeCuO_4$ compound is shown in Fig. 1. This figure reveals good crystallinity with the presence of narrow and strong diffraction peaks. The presence of the strong diffraction peaks corresponding to the crystal planes (111), (220), (311), (222), (400), (422), (511) and (442) indicates the presence of cubic spinel phase. In $Co_{0.5}Ni_{0.5}FeCuO_4$ sample synthesized by sol gel method the result indicates that the diffraction peaks are well defined and correspond in relative height to the peaks reported in the pattern, discarding preferential orientation. Further, the different intensities of the peaks exhibit a sharper and more intense peak which can be related to the higher crystallinity in $Co_{0.5}Ni_{0.5}FeCuO_4$ sample.

The diffraction peak positions and *hkl* crystal planes indexation agree with the JCPDS card No. 10-0325 [10]. From Fig. 1, we can see the formation of pure crystalline phase for $Co_{0.5}Ni_{0.5}FeCuO_4$ spinel ferrite with Fd-3m space group. The lattice constant was calculated from the XRD data using the following equation [11,12]:

$$a = \frac{\lambda}{2}\frac{\sqrt{h^2+l^{2+}k^2}}{\sin\theta} \quad (1)$$

where λ is the X-ray wavelength, a is the lattice constant and (h k l) are the Miller indices. The calculated value of lattice constants of the sample is presented in Table 1. The average crystallite size is obtained from XRD peaks using the Scherer formula as [13]:

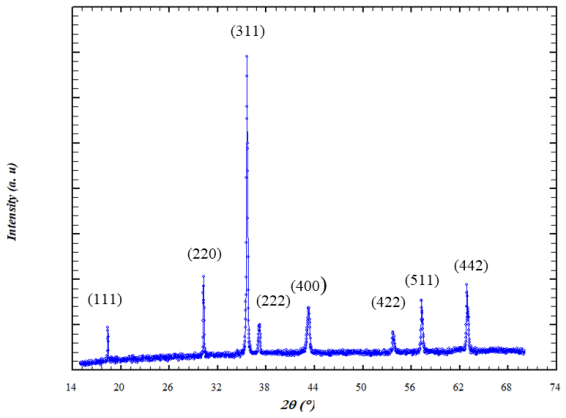

Figure 1. The powder X-ray diffraction pattern of the $Co_{0.5}Ni_{0.5}FeCuO_4$ compound.

Table 1. Structural parameters at room temperature of $Co_{0.5}Ni_{0.5}FeCuO_4$ ferrite.

a (Å)	8.755
V (Å³)	671.114
D_x(g cm^{-3})	5.09
D_b(g cm^{-3})	4.48
P (%)	11.98
D_{XRD}(nm)	47
D_{SEM}(µm)	1.73

$$D = \frac{0.9\,\lambda}{\beta\cos(\theta)} \quad (2)$$

where β is the corrected full-width half maxima of the XRD peaks and θ is the Bragg angle. The estimated value of the average crystallite size is presented in Table 2. The X-ray density of our sample was calculated according to the following equation [10, 13]:

$$D_x = \frac{8M}{Na^3} \quad (3)$$

where M is the molecular weight, N is Avogadro's constant (6.022×10^{23}), and a is the lattice constant. The theoretical density was calculated using the following formula [14, 15]:

$$D_b = \frac{m}{\pi r^2 h} \quad (4)$$

where m, r, and h are respectively the mass, the radius and the height of the sample. The difference between the X-ray density and the theoretical density sets forward the notion of porosity, which is calculated by the following formula [14, 15]:

$$P = \left(1 - \frac{D_b}{D_x}\right) \times 100 \quad (5)$$

2.2. Scanning electron microscopy analysis

The SEM analysis was used to investigate the structural morphology. The SEM micrographs in Fig. 2 show nanoparticles have uniform, almost spherical structural morphology with narrow size distribution. The samples show a grain morphology in which some grains are necked in shape. This necking is attributed to the diffusion between the particles during sintering. We find that this diffusion means smaller particles join together to form the larger one. In addition, the micrographs show inhomogeneous micro-particles with irregular shapes. When the particles adhere to each other, agglomeration occurs, which is due to the dipole-dipole interaction between the particles.

The size distribution of the sample was calculated using image J software. As observed, the histogram

NANOSAM
Journal of NanoScience in Advanced Materials

Table 2. Fitting parameters obtained from experimental data of the total conductivity as a function of frequency and temperature using Jonscher power law: $\sigma(\omega) = \sigma_{dc} + A\omega^n$.

T(K)	σ_{dc} (S/m) ×10^{-4}	A × 10^{-13}	n	χ^2
200	0.00975	4.75	1.12	0.998
220	0.0376	5.12	1.32	0.997
240	0.130	1.356	1.37	0.997
260	0.387	1.372	1.56	0.998
280	1.07	1.108	1.66	0.999
300	2.74	0.89	1.71	0.999
320	6.68	0.741	1.89	0.999
340	153	0.544	2.21	0.997
360	328	0.232	2.33	0.998
380	908	0.159	2.51	0.998
400	1240	0.12	2.78	0.998

is well modeled by Lorentizan fitting as shown in Fig. 3. Summary of the obtained results are shown in Table 2.

The distribution of the elements contained in the synthesized ferrites was further analyzed using EDX. The spectra confirms that the final composition of the samples matches the initial composition and contains no additional impurities. Furthermore, no other impurities can be detected from the EDX spectra indicating the high purity of the prepared samples.

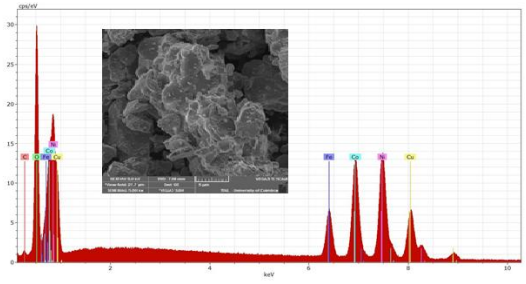

Figure 2. Energy-dispersive X-ray spectroscopy (EDS) analysis of the sample.

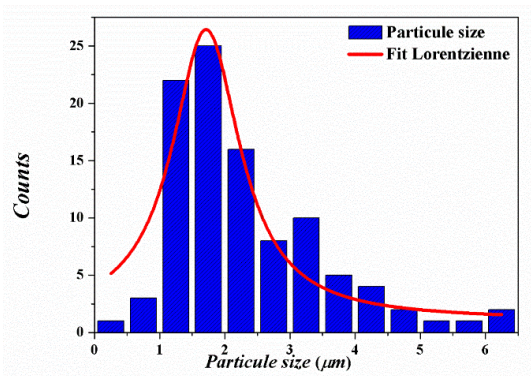

Figure 3. Histogram of $Co_{0.5}Ni_{0.5}FeCuO_4$ nanostructure size distributions determined with Image J software.

2.3. Magnetic characterization

In Fig.4, we presented the variations of M(T) curve under the application of magnetic field of 0.05 T for $Co_{0.5}Ni_{0.5}FeCuO_4$ sample. In this figure, a clear ferromagnetic–paramagnetic (FM–PM) phase transition was observed for the sample at its Curie temperature (T_C). The T_C value estimated from the minimum values of (dM/dT vs. T) curves (see the inset of Fig. 4), is found to be 785 K. For comparison, this T_C value is lower than that obtained for the undoped compound $Ni_{0.7}Cu_{0.3}Fe_2O_4$ (T_C = 823 K) [16, 17]. This result reflects that the substitution of the magnetic Ni^{2+} ion can reduce the Curie temperature of the $Ni_{0.7}Cu_{0.3}Fe_2O_4$ system. It is generally known that the electrical and magnetic properties of ferrites are strongly dependent on the crystallite size. The substitution of ions changes both the crystallite size and the distribution of Fe ions along A and B sites, and thus play an obvious role in controlling and possibly tailoring the electrical and magnetic properties of ferrites.

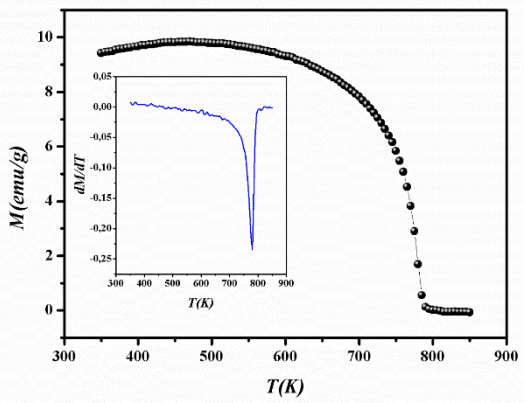

Figure 4. Magnetization curve (M -T) obtained in an applied magnetic field of 0.05 T for $Co_{0.5}Ni_{0.5}FeCuO_4$ sample.

NANOSAM
Journal of NanoScience in Advanced Materials

2.4. Dielectric characterization

The electrical conductivity in the materials is a thermally activated process that takes place due to the ordered motion of weakly bound charged particles under the influence of an electric field. It is one of the significant properties of the materials to be characterized and depends on the nature of charge carriers that dominate the conduction process, such as electron/holes or cations/anions and their response as a function of temperature and frequency. To understand the conduction mechanism and the nature of the electron hopping responsible for conduction, the frequency variation of the conductivity at different temperatures of the sample is shown in Fig. 5. As can be seen from this figure, the conductivity increases with increasing frequency. The dispersion region corresponds to conductivity in the high frequency range. When temperature rises, a sufficient energy probably leads to the hopping of electron density increases between magnetic ions tetrahedral sites (A-sites) and B-sites which conduct to an increment of conductivity [18 43]. Besides, the ac conductivity appeared at high frequencies was caused by heating sample, which leads to increase temperature and a higher energy value need for the progress of mechanism [19 44]. The frequency dependence of conductivity in CFO is known as the sum of these two parts according to Jonscher's power law. As frequency of the applied field increases, hopping of carriers also increases by increasing the conductivity [20].

The total conductivity σ is the superposition of the dc conductivity (σ_{dc}) and the ac conductivity (σ_{ac}) according to the Jonscher's power law given as [21]:

$$\sigma = \sigma_{dc}(T) + \sigma_{ac}(\omega, T) \quad (6)$$

The ac conductivity obeys the empirical formula of the frequency dependence given by the ac power law [21]:

$$\sigma_{ac}(\omega) = A\omega^{n} \quad (7)$$

where A is temperature-dependent constant and n is temperature-dependent exponent that represents the degree of interaction between mobile ions and the lattices surrounding them. The value of n has a physical meaning n < 1 means that the electron hopping involves a translational motion with a sudden hopping, whereas n > 1 means that the motion involves localized hopping between neighboring sites. The exponent n is frequency-independent, but it depends on both temperature and type of material. In this work,the material obeys

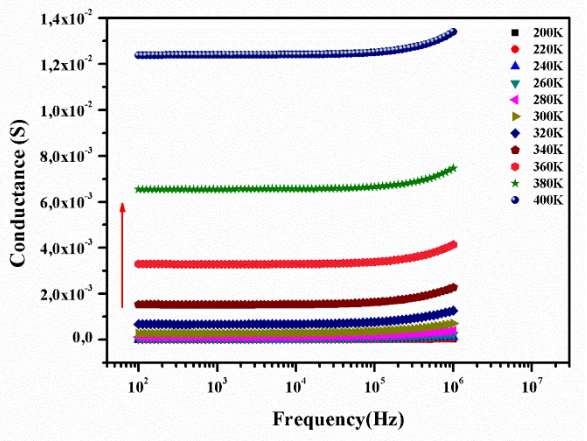

Figure 5. Frequency dependence of total conductivity at different temperatures.

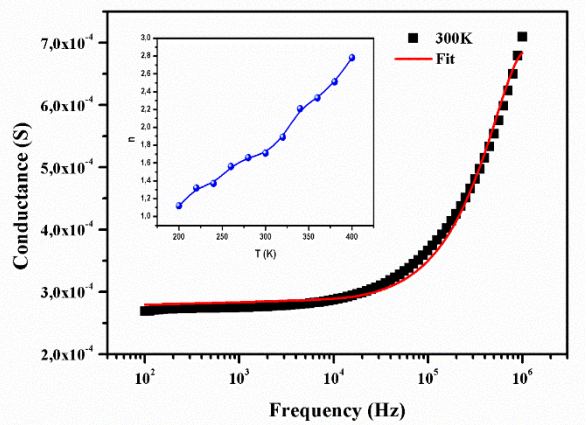

Figure 6. Variation of the conductivity versus frequency at T = 300 K. Red solid line represents the fitting to the experimental data using the universal Jonscher power law. The inset shows the variation of exponent s with respect to all temperatures.

universal power law and is restrained by a typical fit of the above equation. Fig. 6 depicts a typical example of this fitting at T= 300 K. The experimental data of the total conductivity shown in this inset figure were well fitted using Eq. (6) and it is seen that the fit matches well with the experimental data (red solid lines). Therefore, the fitting results at different temperature are summarized in Table. 1. From this table, we can deduce that the exponent n increases with the increasing temperature. This variation of n with temperature corresponds to a thermally activated process. The temperature dependence of n gives information about the mechanism responsible for ac conductivity. In our case, factors A and n were varied simultaneously to obtain the best fit. All values of the n exponent are higher than 1 for all temperatures, indicating that the electron hopping between the cations involves A–B exchange interactions between neighboring sites.

NANOSAM
Journal of NanoScience in Advanced Materials

Fig. 7 shows the plots of the electrical resistivity (ρ) versus temperature deduced from the dc conductivity (σ_{dc}) using the following relation: $\rho = {}^{1}/_{\rho_{dc}}$. This curve indicates that this compound exhibits semiconductor behavior across all the studied temperature ranges. Fig. 8 shows the variation of dc conductivity (σ_{dc}) versus 1000/T used for the calculation of activation energy, and the plot clearly obeys the Arrhenius relation:

$$\sigma_{dc} = \sigma_0 \exp(E_a / k_B T) \quad (8)$$

where σ_0 is the pre-exponential factor corresponding to 1/T=0, k_B is the Boltzmann (k_B = 8,617 ×10^{-5} eV K^{-1}), E_a is the conduction activation energy and T is the absolute temperature. For the sample, the activation energy E_a estimated from the slope of the linear fit plot is equal to 0.42 eV at temperature rang 200-420 K.

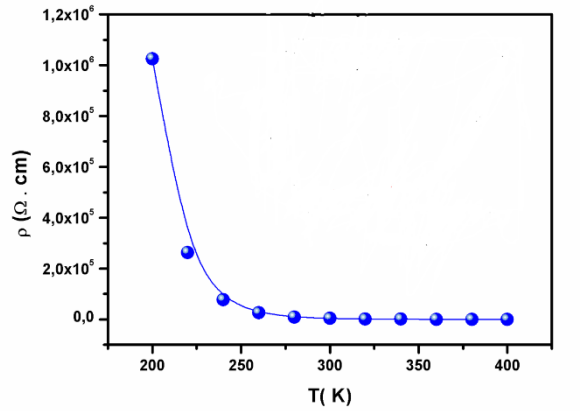

Figure 7. The plot of the electrical resistivity (ρ) versus temperature.

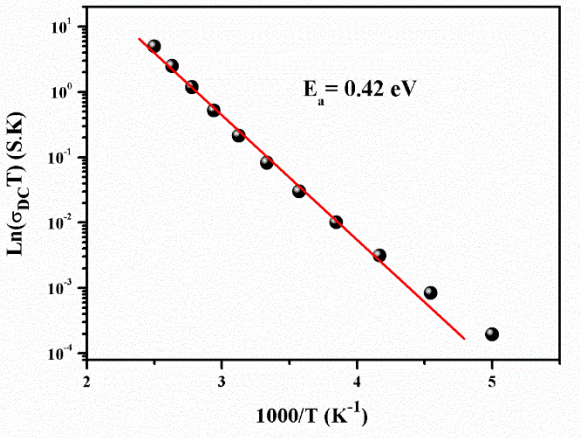

Figure 8. The variation of dc conductivity (σ_{dc}) versus 1000/T.

In order to understand the observed dielectric dispersion, we carried out the complex impedance analysis. The impedance spectroscopy is a very powerful tool for studying the relaxation processes and device structures [22-23]. Complex impedance spectroscopy are carried out in the view of its simplicity and importance in describing the electrical processes occurring in the structure on applying an alternating AC signal across the sample. The yield response of such an experimental measurement, when depicted in a complex plane plot, appears in the form of a succession of semicircles representing the contributions to the electrical properties due to the bulk material, grain boundary effects and interfacial polarization phenomena if any [24,25]. Therefore, in our case impedance analysis is employed to investigate the complex impedance as Z = Z′ + j Z" and dielectric constant as ε = ε′+ j ε" where Z', ε' and Z'', ε'' are the real and imaginary parts of impedance and dielectric constant, respectively. The frequency dependent complex impedance is given by:

$$\mathrm{Re}(Z) = Z' = \frac{\sigma}{\sigma^2 + C^2\omega^2} \quad (9)$$

and

$$\mathrm{Im}(Z) = Z'' = \frac{-\omega C}{\sigma^2 + C^2\omega^2} \quad (10)$$

where C represents the capacitance and ω= 2πf is the angular frequency. On another hand the ε' and ε'' can related with Z' and Z'' by employing the following equations

$$\varepsilon' = \frac{Z''}{wC_0(Z'^2 + Z''^2)} \quad (11)$$

and

$$\varepsilon'' = \frac{Z'}{wC_0(Z'^2 + Z''^2)} \quad (12)$$

where the first term ε' is the real part of dielectric constant representing the amount of energy stored in a dielectric material, while the second term ε'' is the imaginary part of dielectric constant (dielectric loss) which describes the dissipated energy and C_0 is the geometrical capacity.

Fig. 9 shows the variation of the real part of impedance with frequency at various temperatures for the studied sample. The magnitude of Z' decreases with increasing temperature in the low-frequency range which merges in the high-frequency region irrespective of temperature. This behavior can be interpreted by the release of space charge [24]. The reduction in barrier properties of the materials with rise in temperature may be a responsible factor for enhancement of conductance of the materials at higher frequencies [25-26]. However, in the high frequency region this behavior

NANOSAM
Journal of NanoScience in Advanced Materials

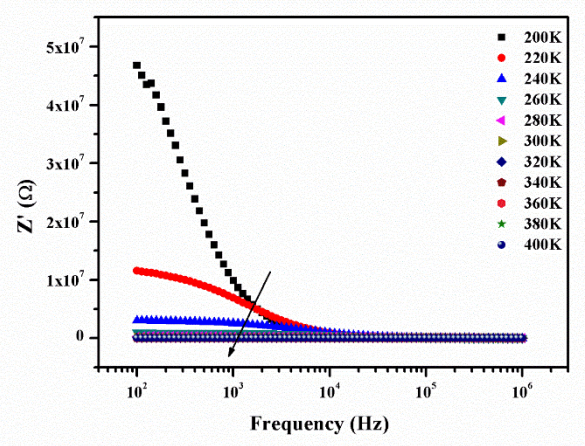

Figure 9. Variation of the real part of the impedance (Z') as a function of frequency for different temperatures.

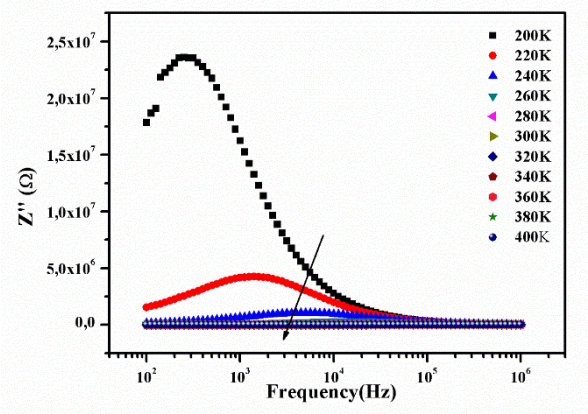

Figure 10. Variation of the imaginary part of the impedance (Z'') as a function of frequency for different temperatures.

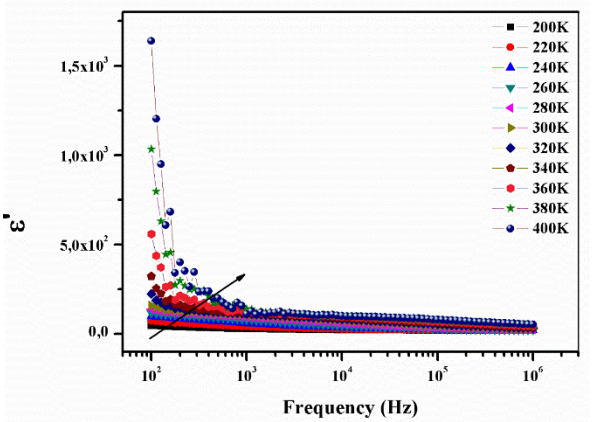

Figure 11. Frequency dependence of imaginary dielectric constant ε' at various temperatures.

is changed considerably showing complete merger of Z' plot above a certain fixed frequency. A particular frequency at which Z' becomes independent of frequency was observed to shift towards the higher frequency side. The shift in Z' plateau indicates the existence of frequency relaxation process in the material. The curves display single relaxation process and show the increase in ac conductivity with increase in temperature and frequency.

The variation of the imaginary part (Z'') with frequency at different temperatures is shown in Fig. 10. These curves exhibit peaks with characteristic frequency maxima which are known as relaxation frequency. A clear broadening of the peaks with increasing temperature indicates the presence of electrical processes in the material with a spreading of the relaxation time. This is can be explained by the presence of immobile species at low temperatures and defects at high temperatures. Since these observations were made at higher temperatures, some relaxation species, such as defects, could be responsible for electrical conduction in the material by hopping of electrons/oxygen ion vacancies/defects between the available localized sites. The heights of peaks are found to decrease gradually with the increase in frequency and temperature, and finally, they merge in the high frequency domain. It indicates the presence of space charge polarization at lower frequencies and disappearance at higher frequencies.

Fig. 12 plots the frequency dependence of imaginary dielectric constant ε'' at various temperatures. It is observed that ε'' has high values at low frequencies, while it decreases with increasing frequency and becomes independent at high frequencies. The observed increase in ε" with temperature at low frequencies could be due to the dipolar polarization facilitating the increase in permittivity [29]. Indeed, the dipoles cannot orient themselves at low temperatures. As the temperature increased and following thermal movements, the orientation of dipoles is facilitated, leading to an increase of dielectric constant value. In the whole explored temperature range, the dielectric constant decreases with increasing frequency. The low value of dielectric constant at higher frequencies is important for extending the material applications towards photonic and electro-optic [30]. The decrease in the dielectric constant with increasing frequency is explained by the decrease of polarization of the dipoles when electric field propagates with high frequency. In other words, beyond a certain frequency of electric field, the charge carrier exchange does not follow the alternating field. The large value of dielectric constant at lower frequency is due to the predominance of species such as oxygen vacancies, grain boundary defects, etc., while the decrease in dielectric constant with frequency is natural because of the fact that any species contributing to polarizability lags behind the applied field at higher

NANOSAM
Journal of NanoScience in Advanced Materials

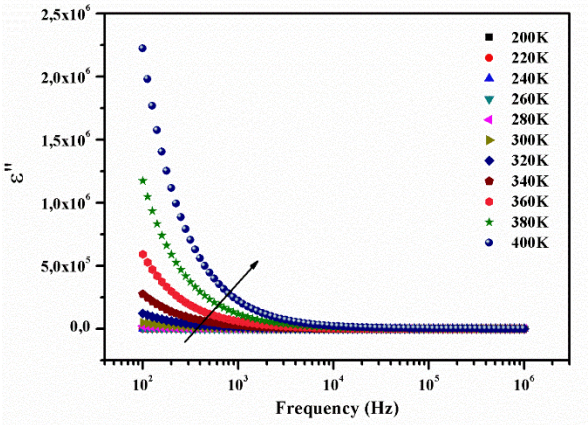

Figure 12. Frequency dependence of imaginary dielectric constant ε'' at various temperatures.

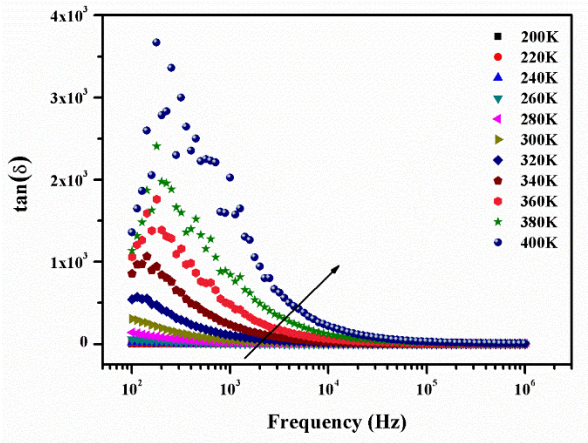

Figure 13. The variation of *tanδ* with frequency.

and higher frequencies [31]. On the other hand, the factor indicating the phase difference due to energy loss within the sample at different frequencies is the loss factor tangent given by [32]:

$$Tan\delta = {Z'}/{Z''} = {\varepsilon''}/{\varepsilon'} \qquad (13)$$

The variation of *tanδ* with frequency is shown in Fig. 13. The dielectric loss increases by increasing temperature at constant frequency. This behavior can be attributed to the fact that at low temperatures, the conduction loss is minimal, when the temperature increases the conduction loss increases due to the increase in conductivity [29, 30]. Furthermore, we can see that, the dielectric loss found to decrease with increasing frequency. This behavior may be due to, in the high frequency, the charge carriers cannot follow the electric field.

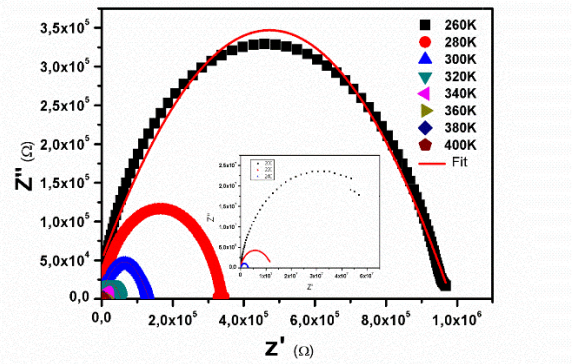

Figure 14. The imaginary part of the impedance (Z'') versus the real part (Z') over a wide range of frequencies and at different temperatures.

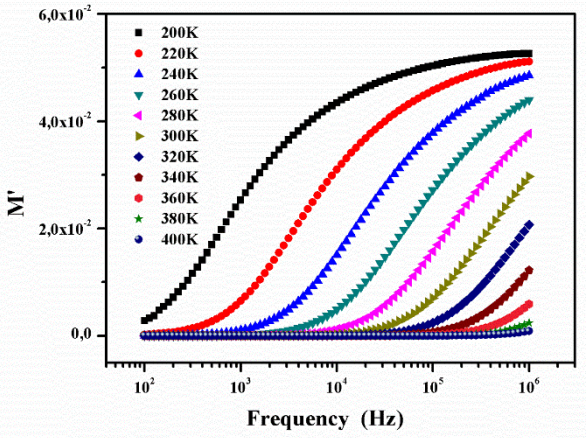

Figure 15. Frequency dependence of the real part of electric modulus (M') at different temperatures.

Fig.14 shows the imaginary part of the impedance (Z'') versus the real part (Z') over a wide range of frequencies and at different temperatures. These plots are characterized by the appearance of semicircular arcs whose maxima decrease with the increasing temperature. The appearance of a single semi-circle at all the temperatures means that the electrical processes obey a single relaxation mechanism [31]. The radius of curvature decreases with the increasing temperature demonstrating a pronounced increase in dc conduction [32-35].

The complex modulus formalism is very convenient tool to interpret the dynamical aspects of electrical transport phenomena. Fig. 15 shows the variation of M' as a function of frequency for the sample at different temperatures. These figures show that M' approaches to zero in the low frequency region, and a continuous dispersion on increasing frequency, with a tendency to saturate at a maximum asymptotic value, in the high frequency region at all the temperatures. Such behavior may be related to a lack of a restoring force governing the mobility of the charge carriers under the action of

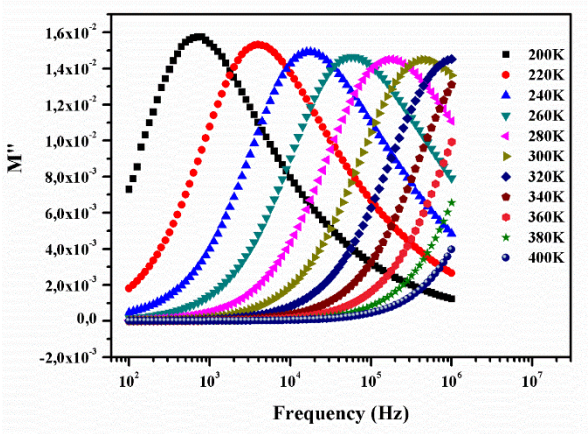

Figure 16. Frequency dependence of the imaginary part of electric modulus (M'') at different temperatures.

an induced electric field. This behavior supports the short-range mobility of charge carrier. Fig. 16 shows the variation of M'' with frequency for the sample at selected temperatures. It is clear from the figures that the modulus spectrum is broader, and the peaks are asymmetric. The peaks shift towards higher frequency side on increasing temperature of the sample. This behavior suggests that the spectral intensity of the dielectric relaxation is activated thermally in which hopping process of charge carriers and small polarons dominate intrinsically.

3. Conclusion

$Co_{0.5}Ni_{0.5}FeCuO_4$ spinel ferrite was synthesized by sol-gel process. The structural study confirms that the material has formed a cubic structure with space group Fd-3m with an average crystallite size of 43 nm. The magnetic measurements were confirmed by axial extraction BS1. The analysis of the magnetic measurements shows that the material exhibits a magnetic transition from the ferromagnetic to the paramagnetic state at the Curie temperature T_C= 785K. The electrical and dielectric properties are analyzed by impedance spectroscopy and found to be dependent on temperature and frequency. The value of the activation energy deduced from the conductivity σ_{ac} is in the order of 0.42 eV, and the sample presents a relaxation phenomenon with non-Debye type.

Method

The $Co_{0.5}Ni_{0.5}FeCuO_4$ ferrite is prepared by sol–gel method using the following precursors: Co $(NO_3)_2.6H_2O$, $Fe(NO_3)_3.9H_2O$ and $Cu(NO_3)_2.3H_2O$ with 99.9% purity and purchased from Sigma Aldrich. In a typical synthesis, stoichiometric amounts of $Fe(NO_3)_3{\cdot}9H_2O$, $Cu(NO_3)_2{\cdot}6H_2O$ and glycine were dissolved in distilled water to give a mixed solution. The initial solution was prepared by mixing distilled water and the nitrates followed by the addition of citric acid ($C_6H_8O_7$) as complexing agent for different metal ions. The solution was heated to 70 °C with thermal agitation followed by the addition of ethylene glycol until a high viscosity residue (gel) was formed. The resulting gel was then heated on a hot plate at 180 °C until a dry foam was formed. This was ground and then annealed at 400 °C to evaporate the organic materials. The resulting black powder was calcined at 700 °C for 24 h to ensure complete release of the organic compounds. After an annealing at 900 °C, the material was subjected to another grinding and annealing cycle until a very fine powder was obtained to obtain the desired phase.

Powder X-ray diffraction (XRD) pattern of the sample was recorded using a D5000 diffractometer with Cu-Kα radiation (λ=0.154060 nm) to check the structure and phase purity. The morphology of the sample was observed by scanning electron microscopy (SEM), using a ZEISS-Ultra+system. Magnetic measurements were realized with the BS1 magnetometer. For the electrical measurement, the obtained powder is sintered in a pellet form of approximately 10 mm of diameter and 2 mm of thickness. We deposited on the both sides of the pellets, a thin silver layer by evaporation under vacuum through a circular mask. This plate capacitor configuration allows the measuring of the electronic transport across the compound and the capacitance. We used an Agilent 4294A analyzer to measure the conductance and the capacitance. To vary the temperature, the sample was mounted on the cold plate of a liquid nitrogen cooled cryostat VPF800 of Janis Corporation. In fact, the temperature was measured by a silicon diode placed near the sample in the cryostat and regulated by the controller 421 of Lakeshore Company. All the measurements were conducted under vacuum and in the dark to avoid the effect of the ambient atmosphere and of the illumination.

Acknowledgements

The authors extend their appreciation to the Deanship of Scientific Research at Jouf University for funding this work through research grant No (DSR-2023-03-02354)

Data Availability Statement

The data that support the findings of this study are available from the corresponding author upon reasonable request.

Authors' contributions:

All authors have equal contribution to this work.

References

[1] Lázár, K., Mathew, T., Koppány, Z., Megyeri, J., Samuel, V., Mirajkar, S.P., Rao, B.S., Guczi, L., Cu1-xCoxFe2O4 ferrospinels in alkylation: structural changes upon reaction, Physical Chemistry Chemical Physics **4** 3530–3536 (2002).

[2] Batoo, K.B., Ansari, M.S., Low temperature-fired Ni-Cu-Zn ferrite nanoparticles through auto-combustion method for multilayer chip inductor applications, Nanoscale Research Letter **7** 112 (2012).

[3] Rahman, M.T., Vargas, M., Ramana, C.V., Structural characteristics, electrical conduction and dielectric properties of gadolinium substituted cobalt ferrite, Journal of Alloys Compounds **617** 547-562 (2014).

[4] Meng, Y.Y., Liu, Z.W., Dai, H.C., Yu, H.Y., Zeng, D.C., Shukla, S., Ramanujan, R.V., Structure and magnetic properties of Mn(Zn)Fe2−*x*RE*x*O4 ferrite nano-powders synthesized by co-precipitation and refluxing method, Powder Technology **229** 270-275 (2012).

[5] Raghasudha, M., Ravinder, D., Veerasomaiah, P., Thermoelectric power studies of Co–Cr nano ferrites, Journal of Alloys Compounds **604** 276–280 (2014).

[6] Dar, M.A., Varshney, D., Effect of d-block element Co^{2+} substitution on structural, Mössbauer and dielectric properties of spinel copper ferrites, Journal of Magnetism and Magnetic Materials **436** 101-112 (2017).

[7] Nikumbh, A.K., Pawar, R.A., Nighot, D.V., Gugale, G.S., Sangale, M.D., Khanvilkar, M.B., Nagawade, A.V., Structural, electrical, magnetic and dielectric properties of rare-earth substituted cobalt ferrites nanoparticles synthesized by the co-precipitation method, Journal of Magnetism and Magnetic Materials **355** 201–209 (2014).

[8] Sun, G.L., Li, J.B., Sun, J.J., Yang, X.Z., The influences of Zn^{2+} and some rare-earth ions on the magnetic properties of nickel-zinc ferrites, Journal of Magnetism and Magnetic Materials **281** 2–3 (2004).

[9] Rezlescu, N., Rezlescu, E., Pasnicu, C., Craus, M.L., Effects of the rare-earth ions on some properties of a nickel-zinc ferrite, Journal of Physics: Condensed Matter **6** 5707–5716 (1994).

[10] Sena, R., Jain, P., Patidara, R., Srivastavab, S., Ranac, R.S., Guptaa,N., Materials Today: Proceedings **750** 757 (2015).

[11] Dinkar, D.K., Das, B., Gopalan, R., Dehiya, B.S., Effects of surfactant on the structural and magnetic properties of hydrothermally synthesized NiFe2O4 nanoparticles, Materials Chemistry and Physics **70** 76 (2018).

[12] Adeleke, J.T., Theivasanthi, T., Thiruppathi, M., Swaminathan, M., Akomolafe, T., Alabi, A.B., Photocatalytic degradation of methylene blue by ZnO/NiFe2O4 nanoparticles, Applied Surface Science **415** 195-200 (2018).

[13] Pottkera, W.E., Onoa, R., Cobosb, M.A., Hernandob, A., Araujod, J.F.D.F., Antonio C.O. Brunod, Lourençoa, S.A., Longo, E., Portaa, F.A.L., Influence of order-disorder effects on the magnetic and optical properties of NiFe2O4 nanoparticles, Ceramics International **44** 14 17290-17297 (2018).

[14] Hcini, S., Omri, A., Boudard, M.,.Bouazizi, M.L., Dhahri, A., Touileb, K. Journal of Materials Science: Materials in Electronics **464** 91 (2018).

[15] Batoo, K.M., El-sadek, M.S.A., Electrical and magnetic transport properties of Ni–Cu–Mg ferrite nanoparticles prepared by sol–gel method, Journal of Alloys and Compounds **566** 112-119 (2013).

[16] Hankare, P.P., Sankpal, U.B., Patil, R.P., Jadhav, A.V., Garadkar, K.M., Chougule, B.K., Magnetic and dielectric studies of nanocrystalline zinc substituted Cu–Mn ferrites, Journal of Magnetism and Magnetic Materials **323** 389-393 (2011).

[17] Ortega, N., Kumar, A., Bhattacharya, P.,. Majumder, S.B, Katiyar, R.S., Impedance spectroscopy of multiferroic PbZr*x*Ti1−*x*O3/CoFe2O4 layered thin films, Phys. Rev. B. **77**, 014111 (2008).

[18] Atiq, S., Majeed, M., Ahmad, A., Abbas, S.K., Saleem, M., Riaz, S., Naseem, S., Microstructural, magnetic and electrical properties of Zn0.4M0.3Co0.3Fe2O4 (M = Ni and Cu) ferrites synthesized by sol–gel method, Journal of Magnetism and Magnetic Materials **43**, 2486 48 (2017).

[19] MacDonald, J.R., Impedance Spectroscopy e Emphasizing Solid Materials and Systems, Wiley, NewYork, 1987.

[20] Jonscher, A.K., Dielectric Relaxation in Solids, Chelsea Dielectrics, London, 1983.

[21] Kumar, A., Singh, B.P., Choudhary, R.N.P., Thakur, A.K., A.C. Impedance analysis of the effect of dopant concentration on electrical properties of calcium modified BaSnO3, Journal of Alloys Compounds **394** 292-302 (2005).

[22] Pradhan, D.K., Samantaray, B.K., Choudhary, R.N.P., Thakur, A.K., Complex impedance studies on a layered perovskite ceramic oxide—NaNdTiO4, Materials Science and Engineering: B **116** 7–13 (2005).

[23] Macedo, P.B., Moynihan, C.T., Bose, R., The Role of Ionic Diffusion in Polarization in Vitreous Ionic Conductors, Physics and Chemistry Glasses, **13**. 171-17913 (1972).

[24] Provenzano, V., Boesch, L.P., Volterra, V., Moynihan, C.T., Macedo, P.B., Electrical Relaxation in Na2O·3SiO2 Glass, American Ceramic Society, **55** 492-496 (1972).

[25] Jain, H., Hsieh, C.H., Window' effect in the analysis of frequency dependence of ionic conductivity, Journal of Non-Crystalline Solids, **172** 1408 (1994).

[26] Hcini, S., Oumezzine, E., Baazaoui, M., Electrical conductance and complex impedance analysis of $La_{0.6}Pr_{0.1}Ba_{0.3}Mn_{1-x}Ni_xO_3$ nanocrystalline manganites, Applied Physics A.**120** 1453–1459 (2015).

[27] Khadhraoui, S., Triki, A., Hcini, S., Variable-range-hopping conduction and dielectric relaxation in $Pr_{0.6}Sr_{0.4}Mn_{0.6}Ti_{0.4}O_3$ perovskite. Journal of Magnetism and Magnetic Materials **371** 69–76 (2014).

[28] Hench, L.L., West, J.K., Principles of Electronic Ceramics John Wiley and Sons, New York, **205** (1990).

[29] Charles, B., Ganam, F.D., Dielectric studies on sodium fluoroantimonate single crystals, Crystal Research and Technology **29** 707-712 (1994).

[30] Bhat, M.H., Kandavel, M., Ganguli, M., Rao, K.J., Li+ ion conductivities in boro-tellurite glasses, Bulletin of Materials Science **27** 189-191 (2004).

[31] Farid, A.M., Bekheet., A.E., AC conductivity and dielectric properties of Sb2S3 films, Vacuum **59** 932 (2000).

[32] El-Nahass, M.M., Ali, H.A.M., AC conductivity and dielectric behavior of bulk Furfurylidenemalononitrile, Solid State Communications 152 12 1084-1088 (2012).

[33] Shukla, A., Choudhary, R.N.P., Thakur, A.K., Thermal, structural and complex impedance analysis of Mn4+ modified

BaTiO3 electroceramic, Journal of Physics Chemistry Solids **70** 1401–1407 (2009).

[34] Johnson, D., ZView: a Software Program for IES Analysis, Version 2.8, Scribner Associates, Inc. Southern Pines, NC (2018).

[35] Hcini, S., Oumezzine, E., Baazaoui, M., Rahmouni, H., Khirouni, K., Hlil, E.K., Oumezzine, M., Electrical conductance and complex impedance analysis of La0.6Pr0.1Ba0.3Mn1−xNixO3 nanocrystalline manganites, Applied Physics A **120** 1453 (2015).